Artificial Vision System for the Automatic Measurement of Interfiber Pore Characteristics and Fiber Diameter Distribution in Nanofiber Assemblies

6 **AUTHORS**, INCLUDING:

Pierantonio Facco
University of Padova
39 PUBLICATIONS **313** CITATIONS

SEE PROFILE

Martina Roso
University of Padova
27 PUBLICATIONS **195** CITATIONS

SEE PROFILE

Michele Modesti
University of Padova
83 PUBLICATIONS **1,404** CITATIONS

SEE PROFILE

Fabrizio Bezzo
University of Padova
104 PUBLICATIONS **1,334** CITATIONS

SEE PROFILE

Artificial Vision System for the Automatic Measurement of Interfiber Pore Characteristics and Fiber Diameter Distribution in Nanofiber Assemblies

Emanuele Tomba,[†] Pierantonio Facco,[†] Martina Roso,[‡] Michele Modesti,[‡] Fabrizio Bezzo,[†] and Massimiliano Barolo*,[†]

Computer-Aided Process Engineering Laboratory (CAPE-Lab), Dipartimento di Principi e Impianti di Ingegneria Chimica, and Dipartimento di Processi Chimici dell'Ingegneria, Università di Padova, via Marzolo 9, 35131 Padova PD, Italy

Nanofiber structures are used in several technologies such as membranes, reinforced materials, textiles, catalysts, sensors, and biomedical materials. For all these applications, it is important to know the morphology of the assemblies, in particular their pore and fiber dimension distributions. However, the current methods used to measure pore sizes are all experimental and indirect; furthermore, the fiber diameter distribution is usually determined manually using a digital image of the nanofiber web. In this paper an artificial vision system is proposed to characterize the nanofiber web by automatically measuring several properties related to the interfiber pore distribution and to the nanofiber diameter distribution. The artificial vision system is characterized by a two-section structure: an image processing section and a property measurement section. The image processing section is centered on a multivariate image analysis procedure for the extraction of morphological features from the image. The property measurement section comprises an algorithm for interfiber pore area and pore morphology evaluation and one for fiber diameter distribution measurement that also accounts for the effect of perspective on the lower-level fiber diameters. Because the proposed artificial vision system is completely automatic, measurements can be taken without the need of any experimental setup and with no human intervention. Therefore, besides being fast and accurate, measurements do not suffer from repeatability issues. The ability of the proposed automatic system in characterizing the morphology of a thin nonwoven nanofiber fabric is demonstrated by application to polymer nanofiber membranes obtained by electrospinning.

1. Introduction

Nanofiber membranes combine the advantage of high total porosity with low dimensions of pores. These peculiar features have been exploited in several applications, such as filtration and separation,[1] catalysis,[2,3] and biomedical materials processing.[4] In addition to this, the nanometric dimension of fibers leads to important advantages, such as increase of the area-to-volume ratio, greater surface functionality, and better mechanical performance. In particular, the dimension of nanofiber diameters is crucial in those applications where high specific area is required, such as in tissue engineering and drug delivery systems,[5,6] for applications in the reinforcement of composite materials,[7] in the production of protective clothing,[8] or in applications as high-sensitivity nanosensors.[9]

The suitability of a nanofiber membrane for the application it has been manufactured for is therefore strongly related to the interfiber pore and the fiber diameter morphologies. However, as in most nanomaterials, these morphologies are difficult to characterize in a systematic way. Measurement instrumentation may not be available or may require processing experimentally a sample of the material being characterized (possibly with destructive tests), and almost invariably calls for human intervention, which may lead to loss of repeatability and possibly large measurement times.

Porosity is measured experimentally by mercury intrusion porosimetry, liquid extrusion porosimetry, or capillary flow porosimetry.[10] Mercury intrusion porosimetry requires pushing mercury through pores in the material, but the high pressure required for this operation may distort the nanofibers, thus compromising the mat morphology. Liquid extrusion porosimetry is suitable for testing nanofiber membranes, but it measures the total pore volume, rather than the pore throat diameter, which instead is the property one is most interested in. Capillary flow porosimetry does provide a simple and nondestructive technique allowing for a rapid and accurate measurement of pore size and distribution.[11] However, being itself an experimental method, operators and time (hence money) are needed; moreover, it is not always accurate and may downgrade the sample.

Contrary to pore size distribution, experimental methods for nanofiber diameter measurement are not available at present. Instead, the fiber diameter size is determined by visual inspection of scanning electron microscope (SEM) images of the nanofiber mat. Typically, the diameter dimension is measured by manually counting the pixels between fiber boundaries after a fiber has been visually isolated by the operator on the image scene.[12] It is therefore clear that this time-consuming procedure is subject to the operator's judgment, is quite prone to measurement errors, and provides hardly reproducible measurements.

The availability of digital microscopic images of complex nanofiber webs provides an attractive basis for the development of an automatic system for nanofiber characterization, where no human intervention is needed. Such an artificial vision system would be nondestructive, i.e., it could capture information from the inspected product without interfering with it, thus avoiding the typical issues of human visual inspection systems. Furthermore, being automatized, it would lead to perfectly reproducible results.

As far as membrane porosity characterization is concerned, She and co-workers[13] applied an image analysis technique to automatically measure the effective pore diameters and their

---

* To whom correspondence should be addressed. E-mail: max.barolo@unipd.it.
† CAPE-Lab, Dipartimento di Principi e Impianti di Ingegneria Chimica.
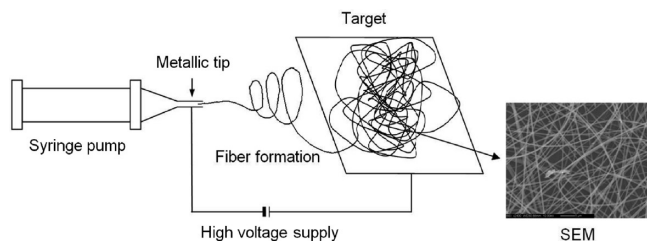‡ Dipartimento di Processi Chimici dell'Ingegneria.

Figure 1. Schematic of the electrospinning process for the production of a nanofiber membrane.

distribution from SEM images of porous filtration membranes (without nanofibers), using the Euclidean distance transform method (EDT). Ziabari and co-workers[14−16] provided a substantial improvement to automatic characterization of electrospun nanofiber morphology. They used image analysis techniques to automatically determine the pore diameter and fiber diameter characteristics of nanofiber structures. However, most of the images they used were simple, simulated ones. Furthermore, such issues as characterizing a multilayer nanofiber web and estimating the effect of perspective correction on such webs were not addressed in their study.

In this paper an artificial vision system is proposed to automatically perform the measurement of the interfiber pore dimension and of the fiber diameter distribution in nanofiber assemblies. The underlying rationale of the proposed method is that the correlation between the intensities of neighboring pixels in an image is closely related to the pore and fiber morphologies. According to this idea, the image can be considered a multivariate system and can be analyzed with multivariate statistical techniques (i.e., multivariate image analysis, MIA) to extract the morphological information embedded within. This information is subsequently quantified through a proper measurement algorithm.

MIA is extremely efficient in extracting and isolating specific image features in a low-dimension subspace called "score space".[17] When a feature is detected in this subspace, MIA can be used to reveal the locations where this feature occurs in the original high-dimension scene space. Then, a metrology algorithm can be used to characterize the isolated feature within the scene space. This approach has led to significant benefits in the chemical process industries in a variety of applications, ranging from process monitoring[18−21] to product quality control and defect detection.[19,22,23]

The ability of the proposed automatic system in characterizing the morphology of a nanofiber web is demonstrated by application to polymer nanofiber membranes obtained by electrospinning. The resulting mats have a quite complex structure, where nanofibers are not straight and are distributed over several layers, which sets a significant challenge in automatic morphology characterization.

2. Nanofiber Membrane Manufacture

The nanofiber membranes considered in this work have been obtained by electrospinning. By this processing technique one can process a vast array of inorganic or hybrid materials, and organic polymers in order to tailor the resulting membrane to the specific application it must be manufactured for. Electrospinning exploits electrostatic forces to produce fibers with diameters ranging in the nanometer scale by forcing a solution through a spinneret under the influence of an electric field (Figure 1). Details on how this technique works can be found elsewhere.[24,25]
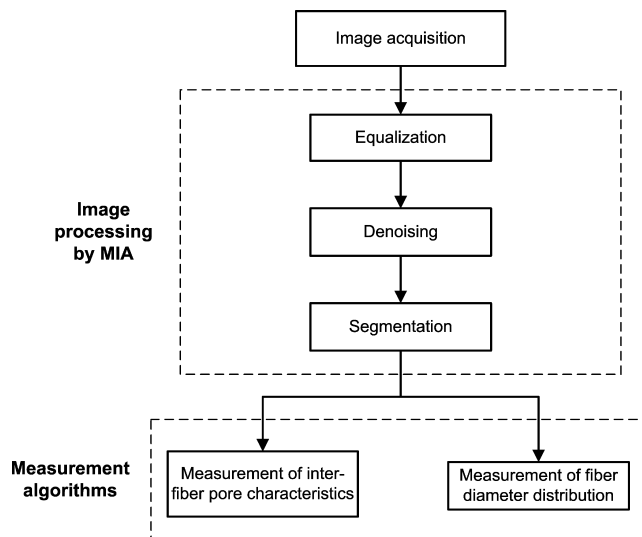

Figure 2. Concept flowchart of the artificial vision system.

The artificial vision system developed in this study was tested on polymer nanofiber membranes.[3,26,27] Poly(acrylonitrile-*co*-vinyl acetate) electrospun fibers were obtained by performing electrospinning of a 12 wt % polymer solution in *N,N*-dimethylformamide fed at 1 mL/h and 26 °C, with a 15 kV applied voltage and at 25×10^{-2} m tip−collector distance. The needle size was 0.4×20 mm. Different types, shapes, and sizes of target have been used. The electrospun samples were characterized by scanning electron microscopy (Obducat Cam-Scan MX2500; Cambridge, U.K.). The SEM images have a resolution of 1024×1280 pixels.

## 3. Development of the Artificial Vision System

To measure the pore and fiber characteristics automatically, an artificial visual inspection system based on multivariate image analysis coupled to an advanced measurement algorithm has been developed. A simplified description of how the system works is shown in Figure 2.

A typical grayscale SEM image of the nanofiber web resulting from the electrospinning process is shown in Figure 3a. The scale of the image is such that 1 pixel corresponds to ~38.5 nm. For ease of discussion, in the remainder of the paper the reasoning will be based on the image of Figure 3a. However, the artificial vision system that has been developed is completely general and can be applied to any other image of the manufactured product.

As a first operation, the image needs to be cropped so that the figure label and calibration bars are removed, and only the membrane surface scene is left for further processing. The cropping operation results in a 984×1280 pixel image. The resulting grayscale image can be thought as a collection of pixels, in which each pixel is highly correlated to its neighbors. The correlation structure can be revealed using MIA techniques. In the next subsections, details are provided on how the image analysis and measurement algorithms work.

One basic assumption that was considered in the development of the automatic measurement algorithms (both for pore area measurement and for fiber diameter measurement) is that the membrane is homogeneous, that is, the analyzed image is representative not only of any location on the membrane surface, but also of fiber layers that are deposited at a deeper level, which cannot be reached by SEM.

3.1. Image Equalization. Equalization is needed because, as can be seen in Figure 3a, the original image may not display
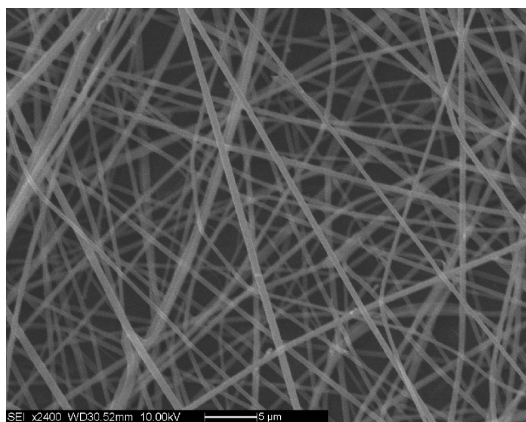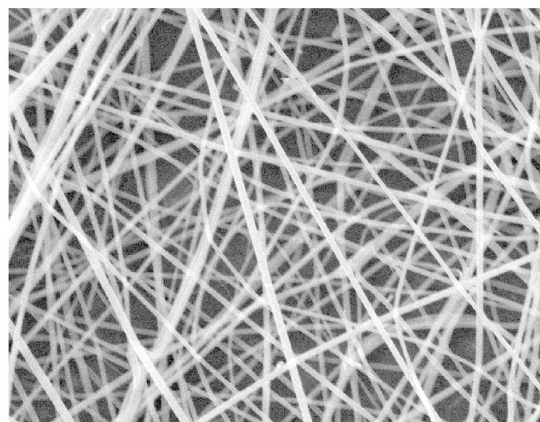
(a)   (b)

Figure 3. SEM micrograph of a polymer nanofiber membrane sample: (a) original image; (b) the same image after cropping and equalization.

a suitable contrast. Enhancing the pixel contrast by equalization is important because it is the difference in the pixel intensities of pores and fibers that allows carrying out the discrimination between pores and fibers automatically. In this work equalization consisted in remapping the light intensities to cover the whole range between 0 and 255. A nonlinear equalization was applied by weighting the higher intensities more, in such a way as to emphasize the fiber pixels more markedly than the pore pixels. In this way, the brightness of image was increased and further fibers could be distinguished that were somewhat hidden in the original image, mostly because they were lying underneath the most visible layer (Figure 3b). However, this kind of equalization also involves noise amplification. Since the pixel intensities of these "additional" fibers may be comparable to those of noise pixels, increasing the brightness of the image may also increase the noise embedded in the image. Typically, this results in the presence of blurry or incomplete objects in the image scene that can be classified as noise.

3.2. Image Denoising. To reduce the effect of noise, regardless of its origin, a wavelet filter was applied.[28] By this multiresolution approach, the image scene is examined by decomposing it at different resolution scales (spatial frequencies).[29] Subsequently, the image is recomposed to get an approximation of the original one, resulting from the combination of different scale-dependent functions (wavelets). At each decomposition level m, an approximation image $\mathbf{I}_m$ and a detail image $\mathbf{D}_m$ are identified, which are representative respectively of the lower and higher frequency contents of the signal. Image $\mathbf{I}_M$, which is the denoised version of the original image $\mathbf{I}_0$ at decomposition level M in the domain of the pixel space, is obtained by subtracting from the original image all the high-frequency elements of the decomposition:

$$\mathbf{I}_M = \mathbf{I}_0 - \sum_{m=1}^{M} \mathbf{D}_m \qquad (1)$$

where

$$\mathbf{D}_m = \mathbf{D}_m^h + \mathbf{D}_m^v + \mathbf{D}_m^d \qquad (2)$$

and $\mathbf{D}_m$ is the sum of the horizontal $\mathbf{D}_m^h$, vertical $\mathbf{D}_m^v$, and diagonal $\mathbf{D}_m^d$ details.[30] The details at decomposition scales lower than M account for higher frequencies; consequently, they are related to noise and should be removed, being a nonsystematic fraction of the image signal. The issue to be resolved for the application
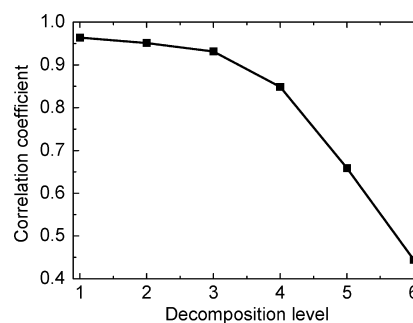

Figure 4. Correlation coefficient between the original image and the denoised one as a function of the decomposition level.

of this approach is the selection of the appropriate decomposition level M: if M is too low, insufficient filtering is applied, whereas if M is too high, the filtering action is so heavy that also systematic portions of the signal are removed.

The most appropriate decomposition level was determined as the one for which a change in the trend of the correlation coefficient between the original image $\mathbf{I}_0$ and the denoised one $\mathbf{I}_M$ was shown.[31] To apply this approach, the denoised image is represented at increasing decomposition levels; that is, details at decreasing frequency scales are subtracted from the original image, as shown in eq 1. This amounts to discarding the highest frequency portion of the image signal first, then the second highest, and so on. By increasing the decomposition levels while discarding the higher frequencies, filtering becomes heavier and heavier until the original image characteristics are lost, because of an excessive smoothing action. The amount of structural information lost because of smoothing can be quantified by the correlation between the original image and the filtered one, which decreases as the filtering action becomes heavier. Figure 4 shows that, for a decomposition scale larger than 3, the correlation coefficient between the original image and the denoised one drops appreciably. To avoid the risk of excessive smoothing, $M = 2$ was selected in this study. This choice was also confirmed by maximizing the Shannon entropy as suggested by Addison[28] and recently applied also by Sun and co-workers.[32]

As for the type of wavelets to be employed, Daubechies wavelets with eight scaling coefficients were selected.[28] The use of this type of wavelet is suggested especially for texture analysis, surface analysis, and image denoising.[33] Moreover, Daubechies wavelets respond very well to the requirements discussed by Ruttiman and co-workers.[34]

3.3. Image Segmentation. Segmentation is the operation through which the objects one is interested in (i.e., fibers and pores) are automatically localized in the (filtered) image scene. To achieve this goal, MIA techniques were used.

3.3.1. Multivariate Image Analysis. The goal of MIA is to extract significant information (features) from an image reducing at the same time the image data dimensionality. This can be done by performing multiway principal component analysis (MPCA) on a multivariate image.[35] MPCA linearly combines the original variables (i.e., pixel intensities) into a reduced number of fictitious variables, called principal components (PCs) or latent variables, which best explain the data variance by identifying orthogonal directions of greatest variability in data. This way, highly correlated data are projected onto a reduced dimension latent subspace (called score space) through a few linear combinations of them.

A multivariate image is a collection of congruent two-dimensional images of the same scene, where each image $\mathbf{I}$ has dimension $[I \times K]$ and represents a unique variable (for example, a spectral variable such as color in RGB images). This collection is arranged in a three-dimensional array $\underline{\mathbf{X}}$ $[I \times J \times K]$, where J is related to the variable which differentiates the images among each other. MPCA decomposes such a three-dimensional array into A principal components, consisting of score matrices $\mathbf{T}_a$ $[I \times 1 \times K]$ and loading vectors $\mathbf{p}_a$ $[1 \times J]$, plus a residual array $\underline{\mathbf{E}}$ $[I \times J \times K]$:[18]

$$\underline{\mathbf{X}} = \sum_{a=1}^{A} \mathbf{T}_a \otimes \mathbf{p}_a + \underline{\mathbf{E}} \tag{3}$$

where "$\otimes$" denotes the Kronecker product. The score matrices $\mathbf{T}_a$ have the same size as the original images and can be interpreted as latent variable images of the original image space.

The PCs are so extracted that the first PC explains the greatest part of the variance in $\underline{\mathbf{X}}$, the second PC the next greatest variance, and so forth. Usually, only a few PCs are required to extract most of the meaningful information from $\underline{\mathbf{X}}$.

MPCA is equivalent to unfolding the three-way array $\underline{\mathbf{X}}$ into a two-dimensional matrix $\mathbf{X}$ $[(I \cdot K) \times J]$,[36] and then performing an ordinary PCA on it:

$$\underset{I \times J \times K}{\underline{\mathbf{X}}} \xrightarrow{\text{unfolding}} \underset{(I \cdot K) \times J}{\mathbf{X}} = \sum_{a=1}^{A} \mathbf{t}_a \mathbf{p}_a^{\mathrm{T}} + \mathbf{E} \tag{4}$$

where $\mathbf{t}_a$ $[I \cdot K \times 1]$ is a score vector, and $\mathbf{p}_a$ $[J \times 1]$ is a loading vector. The unfolding is carried out by stacking the vertical slices (dimension $[I \times J]$) of the three-way array one underneath the other along the J dimension. The columns of $\mathbf{X}$ are built in such a way as to provide information on the spatial correlation of each pixel in an image with its neighboring ones. To this purpose, the algorithm of Bharati and co-workers[20] was used. Details of this algorithm can be found in the original reference. Here, it suffices to say that eight additional two-dimensional images are built by shifting $\mathbf{I}$ by one pixel in eight directions, so that a $[3 \times 3]$ neighborhood of each pixel is considered. The $J = 9$ resulting images are put side by side to form the three-way array $\underline{\mathbf{X}}$. Therefore, the dimension J of $\underline{\mathbf{X}}$ represents a spatial variable (the spatial shift index), and this information (which is related to image morphology) is preserved when carrying out MPCA onto this array.

3.3.2. Application of MIA to Nanofiber Membrane Images. The resulting three-way array to be analyzed by MPCA has the dimension of ($982 \times 9 \times 1278$) pixels. Figure 5 shows the images of the first four scores of the denoised image (for
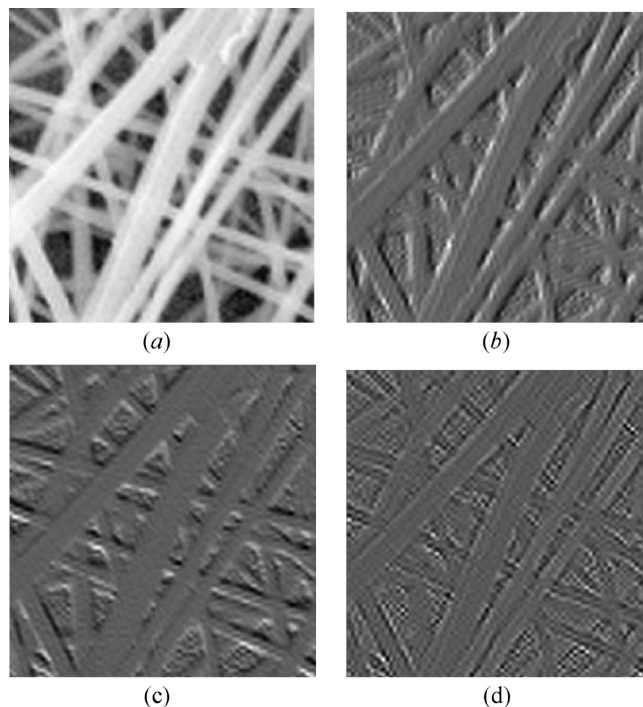

Figure 5. Images of the scores obtained from MPCA applied to the denoised image: (a) $\mathbf{T}_1$; (b) $\mathbf{T}_2$; (c) $\mathbf{T}_3$; (d) $\mathbf{T}_4$. Only 1/12 of the original image has been considered to improve readability.

Table 1. Variance Captured by Each PC on the Denoised Image

principal component	this PC (%)	total (%)
1	97.438	97.438
2	1.479	98.917
3	0.989	99.906
4	0.059	99.965
5	0.021	99.986
6	0.010	99.996
7	0.001	99.998
8	0.001	99.999
9	0.000	100.000

clarity, only 1/12 of the original image is represented). By the visual inspection of these images one concludes that the first PC (PC1; Figure 5a) mainly explains the average pixel intensities over their local area in the multivariate image;[20] i.e., PC1 serves as a smoothing filter on the nanofiber membrane image. The second and third PCs (Figure 5b,c) mainly extract information related to the fiber edges (on different directions), while the fourth PC (Figure 5d) does not add substantially different information, being mostly representative of noise.

This is also confirmed by Table 1, where the contribution of each PC to explaining the total variance of the three-way image is reported. Almost all of the variance is captured by the first principal component, and the fraction of variance added up by the PCs larger than 3 is hardly noticeable. Therefore, almost all of the systematic variation in the image scene (fibers; pores) can be reconstructed by only three principal components in the score space, whereas all the other PCs are mostly descriptive of random variability (noise).

So far, MIA has been applied only to provide a reduced-dimension version of the original image (while maintaining spatial information), but the identification of pores and fibers in the image scene (i.e., image segmentation) is still an open issue. However, note that the image scores are the projections of the pixel intensities onto the principal component subspace. This means that for each pixel in the image scene a set of score values, which can practically be reduced to the pair (t_1; t_2), can
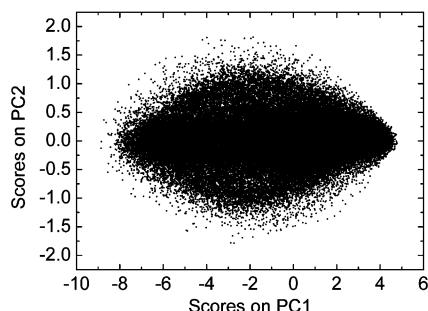
Figure 6. Score plot for the denoised image. Only 1/12 of the original image has been considered to improve clarity.

be calculated that represents the summary of the dominant spatial features in that pixel neighborhood. The score value combination $(t_1; t_2)$ would be almost identical for the pixels that represent the same feature in the image scene (e.g., a fiber point located on a given layer or a pore). Therefore, the score combination of all pixel locations in the image scene space having the same correlation characteristics would plot in the same neighborhood on the score plot, i.e., on a scatter plot where the scores are plotted one against the other.[18]

Figure 6 shows the resulting score plot (again, reference is made to only 1/12 of the image scene for clarity). It is clear that it is the first PC that provides the main discrimination between the correlation characteristics of the pixels. The score point density seems to indicate that the score points are mainly clustered in the score plot locations with $-2 \leq PC1 \leq 4$. By using standard masking procedures, it can be shown that pixels representing fibers are associated with this cluster, which is consistent with the fact that the number of pixels representing the fibers is much larger than that representing the pores in the membrane analyzed. However, this cluster identification procedure is quite subjective, particularly so if it is to be extended to the whole image scene. Furthermore, the procedure is not able to identify which layer in an image scene a fiber belongs to.

As an alternative, cluster identification can be done automatically by cluster analysis. Automatic cluster identification in the score space can be obtained using a k-means algorithm.[37] This algorithm requires as input the number of clusters to be identified, and returns as output the membership of each score point to any of the selected clusters. Let us first examine the results for an assigned number of six clusters. How this number can be determined will be discussed shortly.

Figure 7a shows the scatter plot of the first two PCs, represented as a three-dimensional histogram. The x and y axes represent the score coordinates, whereas the z axis corresponds to the total number of pixels projecting onto a given point of the score plane. The clusters identified by the k-means algorithm are indicated by different colors in Figure 7a. After the clusters have been identified, each point on the score plane can be projected back onto the image scene maintaining the color of the cluster it belongs to (Figure 7b). The following can be observed:

- The first PC is responsible for cluster segregation (Figure 7a).
- Cluster segregation occurs on the basis of pixel intensity (Figure 7a and 7b).
- The clusters to which the largest fraction of pixels (∼50%) belong are the yellow one and the magenta one (Figure 7a).
- These two clusters correspond to fibers located in the foreground of the image scene, and some of these fibers seem to overlap (Figure 7b).

- The green and red clusters represent fibers located on underneath layers (Figure 7b); about 30% of all pixels belong to these clusters.
- The blue and gray clusters collect the remaining 20% of pixels, belonging to the background (pores) or possibly to farther fiber layers, which are hardly distinguishable to the naked eye (Figure 7b).

It can be concluded that the different clusters detected in the scatter plot of the first two PCs can capture the three-dimensionality of the membrane. This is very important for the measurement of the fiber diameter, because the segmentation of different fiber layers allows consideration of the effect of image perspective on the measured diameter value. Finally, it should be noted that, because MPCA provides information on the spatial correlation of each pixel in an image with its neighboring ones, segmenting the image in the score space rather than directly in the scene space provided a further filtering to the image and allowed for a better identification of fibers and pores.

3.3.2.1. Determination of the Optimal Number of Clusters. The number of clusters to be input to the cluster analysis algorithm depends on the type of membrane being analyzed. Namely, it was found that the larger the fiber density, the larger the number of clusters to be considered. The procedure for optimal cluster number determination is a sequential one, starting with two clusters and progressively increasing this number by one until an assigned condition is met on the image correlation. The two images to be compared are the original (denoised) one and the image reconstructed using the current number of clusters. Image reconstruction is carried out according to this criterion:

- The pixels belonging to the clusters associated with the two lowest intensities are always associated with the background and are therefore reconstructed in black.
- The pixels belonging to the remaining clusters are reconstructed with the same intensities as in the original image.

The plot of the correlation coefficient for the original denoised image and the reconstructed one for different numbers of clusters is shown in Figure 8. It can be noticed that for a number of clusters larger than six the correlation between the two images is not improved. This means that there is no incentive to segment further fiber layers any more through the definition of additional clusters.

3.4. Pore Relative Open Area Measurement. The relative open area (ROA) of pores is the ratio between the pore open area and the total area. Although ROA is not equivalent to porosity (which is defined on a volume basis, and is the very property one is interested in), it has been shown[38] that a linear correlation exists between ROA and porosity for woven fabrics. For thin nonwoven nanofiber membranes like those considered in this study, it is reasonable to assume that the mat has a high packing density. Therefore, under this assumption, for such membranes a porosity measurement can be directly related to a pore open area measurement. In this subsection, a method for the automatic measurement of pore open area is presented.

Pore open area is directly related to the amount of background pixels in the image scene. Therefore, to obtain a pore area measurement from an image, one only needs to discriminate between background and fibers, regardless of the layer a fiber is lying on. To perform a pore area measurement, a binary (i.e., black and white) image is therefore sufficient, where fiber pixels can be represented in black and the background ones in white. As mentioned in section 3.3.2.1, the two clusters whose pixels have lower intensities were assigned to image background and
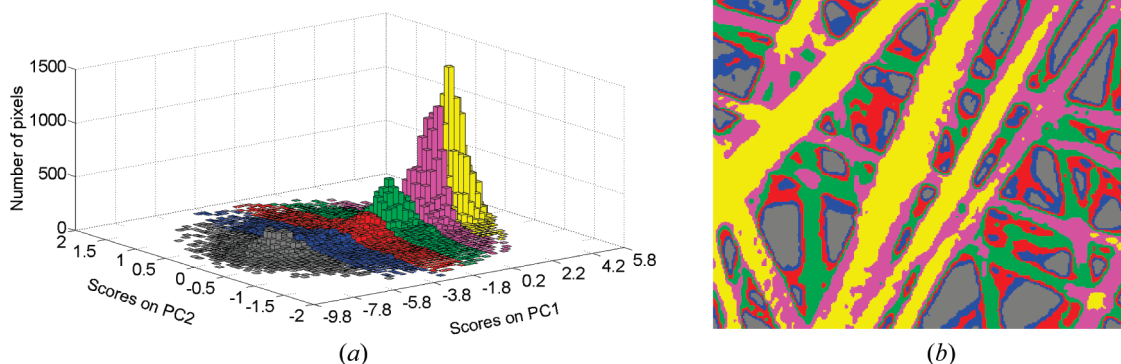
Figure 7. (a) Histogram score plot after application of the cluster analysis algorithm. The histogram represents the number of pixels having the same projections (t_1; t_2) on the score plot. (b) Representation in the image scene of the clusters identified by cluster analysis. Only 1/12 of the original image has been considered to improve clarity.
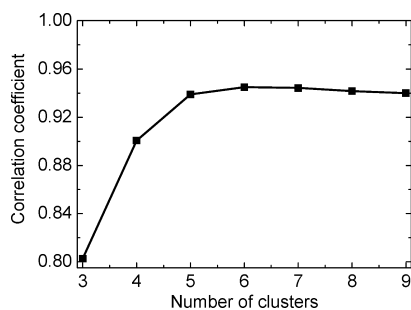

Figure 8. Determination of the optimal number of clusters: correlation coefficient between the original image and the image reconstructed with different numbers of clusters.

Figure 9. Final image on which pore morphology measurements were taken.

were therefore white colored. All of the other pixels were assigned to fibers and colored in black.

It may happen that some incomplete portions of fibers lying underneath the visible layers show up (normally as small isolated black blobs) after image segmentation and binarization have been carried out. This is due to the fact that an SEM micrograph can completely detect the upper-fiber layers only. Other layers may however be present under those visible in the SEM image, and image segmentation may make limited portions of these lower-layer fibers visible by separating them from the background.

Before evaluating the pore morphology, two further operations are therefore required on the binary image. The first one is a morphological operation through which the isolated black pixel blobs discussed above are erased from the white regions within which they appear. This operation acts as a further image filtering. The second operation is the "blackening" (i.e., exclusion) of pores connected to the edge of the image frame. In fact, because these pores are incomplete, their shape parameters are meaningless.[13] The resulting image is shown in Figure 9. The pore (i.e., white) regions are eventually identified on this image, and they are labeled to automatically measure their geometric properties.

ROA can be simply defined as the ratio between the number of white (i.e., background) pixels and the total number of pixels (note that edge pore blackening is actually carried out only after the value of ROA has been determined). In addition to ROA, the pore regions can also be characterized by a set of numerical parameters using standard measurement algorithms.[39] These parameters are the following:
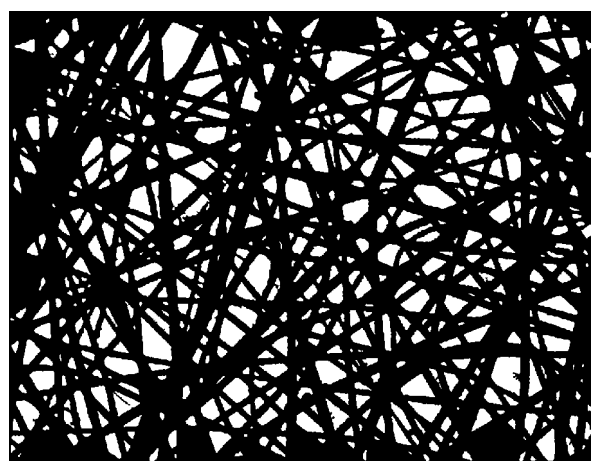
- Pore hydraulic diameter, i.e., the ratio between the pore area and the pore perimeter.[40]
- Pore equivalent diameter, i.e., the diameter of a circle with the same area of the region.
- Lengths of the major and the minor axes of the ellipse having the same normalized second central moment as the pore region.

Because all the measurements were given in pixel units, they were transformed into nanometers using the calibration bar given in the original image. It should be noted that an image scene dimension appropriate with respect to the expected pore dimension should be used. In fact, when very large pores are expected and the image scene is too small, the number of pores visible for analysis might be statistically insufficient and measurement repeatability issues may arise.

3.5. Nanofiber Diameter Measurement. Measuring the diameter in a nanofiber web as complex as that shown in Figure 3 is challenging for several reasons. First, the fibers are deposited onto several layers and, due to perspective effects, in the image scene the lower-layer-fiber diameters appear smaller than they actually are. Second, not only do fibers cross each other, but some of them may even overlap for quite a long segment. Third, several fibers are not straight within the image scene.

In this study the first problem was addressed by assuming that the membrane is homogeneous. Therefore, only the diameter of the upper-layer fibers was measured, assuming that the

diameter distribution of lower-layer fibers was the same as the upper-layer ones. As was shown earlier, the first two score point clusters (i.e., the yellow one and the magenta one) represent fibers lying on the first and second layers. Therefore, after segmentation, the image scene was binary-reconstructed by considering only the fibers belonging to these two clusters; all the other pixels were blackened. Perspective correction was then applied to "move" the second-layer fibers up to the first layer.

The fact that fibers may not only cross, but also partially overlap, is a challenge because this makes the fiber edge difficult to localize using existing automatic procedures for diameter measurement.[14,15] In this study this issue was addressed by developing a fiber segmentation algorithm that allows identification of each single fiber on a layer, regardless of the fact that this fiber partially overlaps or intersects with one or more other fibers. This algorithm works under the assumption that the fibers are almost straight within the inspected image, which is definitely not the case for a real-world nanofiber membrane. Therefore, the fibers displayed in the image were "linearized" by dividing the original image into 48 equal portions (subimages). Within each of these subimages, the fibers are sufficiently straight for the algorithm to work with good accuracy.

The fiber detection and segmentation algorithm is the core of the measurement algorithm. The basic principle under which a single fiber is detected on the subimage scene is the following: a fiber in the subimage scene can be represented as ("filled with") a series of parallel straight segments connecting two adjacent or opposite edges of the subimage, with the direction of the segments being the same as the fiber axis direction. Once a fiber has been represented on the subimage scene using this criterion, the fiber diameter is measured as the Euclidean distance (in pixels) between the two limiting segments.

The measurement algorithm proceeds in six sequential steps, which are described in the following. Further details are provided by Tomba.[41]

3.5.1. Step 1: Fiber Linearization. The binary image is divided into 48 subimages (162 × 158 pixels each), which allows approximating as a straight line each single fiber appearing in a subimage. Note that the larger the number of subimages, the more reasonable is the straight-line approximation, but the larger the subsequent computational time. Also note that since a fiber may appear in several subimages, the partitioning in subimages allows having more than one diameter measure for each nanofiber. An example of the analyzed subimages is given in Figure 10a.

3.5.2. Step 2: Fiber Detection. Fibers are identified as a collection of straight segments connecting any two subimage edges and crossing white pixels only. Starting from the upper subimage edge, all white pixels are first detected on it; then, each of them is connected to all the white pixels on the other edges using straight segments. Any such segment may cross black and white pixels belonging to the subimage interior. Therefore, a segment is deemed a potential fiber (and its location on the subimage saved for further analysis) if either (i) it crosses white pixels only in the subimage interior or (ii) for each black pixel it crosses at least one of the two pixels following the black one within the segment is white. This procedure is automatized by always drawing the segments from the upper edge to the right one and to the opposite one; after these three edges have been scanned, the subimage is rotated counterclockwise by 90°, and the procedure is iterated until all possible edge combinations are completed. Figure 11 shows a flowchart of the fiber detection algorithm.
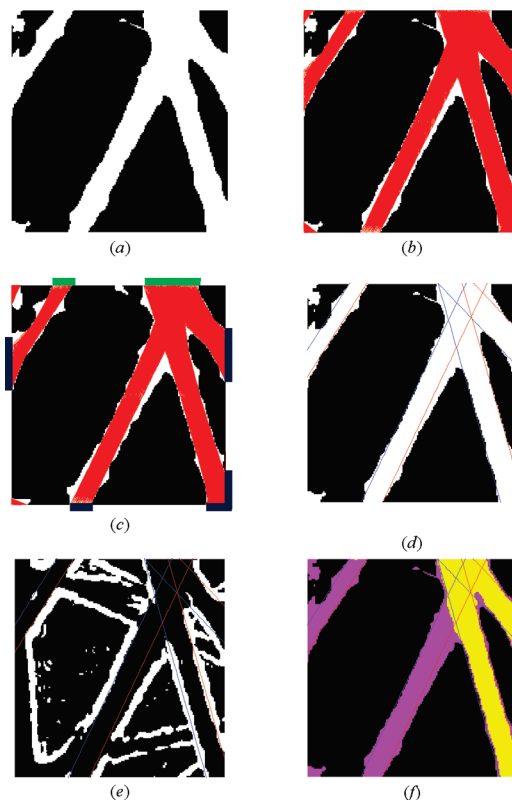

Figure 10. Subimages obtained during the application of the algorithm for fiber diameter measurement. (a) Step 1: subimage with fibers belonging to the first two clusters. (b) Step 2: detection of fibers by filling fiber areas with straight segments. (c) Step 3: single fiber segmentation. (d) Step 4: identification of fiber axis and preliminary diameter measurement. (e) Step 5: boundary correction. (f) Step 6: perspective correction.

The result of these operations is shown in Figure 10b, where the segments are indicated in red (note that the individual segments cannot be clearly identified in the picture due to their huge number). These segments give rise to a number of red "bands" (not yet to be identified as fibers) within the subimage, possibly crossing and/or overlapping with one another. Note that segments connecting corner white pixels (like those in the lower-right angle of Figure 10a) are discarded because usually they are not representative of a fiber.

3.5.3. Step 3: Single Fiber Segmentation. In this step any single fiber is identified within each of the existing red bands. A fiber is identified as the portion of red band connecting a red strip on one subimage edge (starting strip) to a red strip on a different subimage edge (ending strip). In order to consider all possible subimage edge combinations, the procedure is automatized as in step 2. A graphical representation is shown in Figure 10c, where the starting strips have been highlighted in green and the ending strips have been highlighted in blue. Note that the right green strip is the starting point for three different fibers; each of them can be easily singled out on the basis of the location of the ending strip.

At the end of this step each fiber is associated with a number of segments having different directions.

3.5.4. Step 4: Identification of Fiber Axis Direction and Preliminary Diameter Measurement. The fiber axis direction and the preliminary fiber diameter measurement are determined in this step for each of the fibers identified at the previous step. For any segment within a fiber, the segment is left-shifted until it crosses a sequence of at least three black pixels; this point is assumed to correspond to the left edge of the fiber. Then, from this position the segment is shifted to the right until a sequence
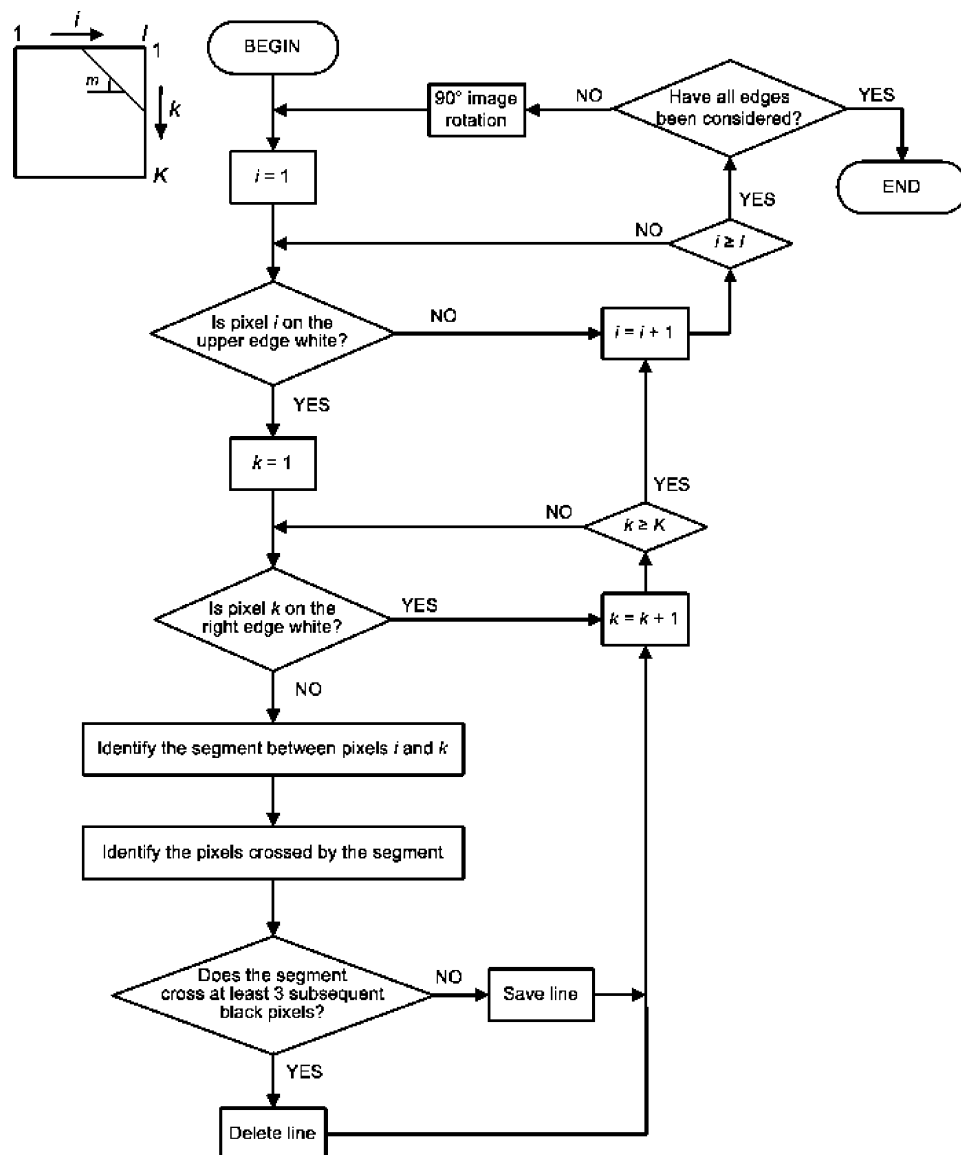
Figure 11. Flowchart of the fiber detection algorithm (step 2). To improve clarity, the detection procedure for adjacent edges only is represented.

of at least three black pixels is crossed, which is assumed to be the right edge of the fiber; the length of the right shift is recorded. The fiber axis direction is assumed to be the segment direction allowing for the maximum right-shift length. The preliminary fiber diameter measurement is determined as the orthogonal distance between the two fiber boundaries corresponding to the selected fiber direction (Figure 10d).

3.5.5. Step 5: Identification of True Fiber Boundaries and Diameter Measurement Correction. A correction to the measured fiber diameter is carried out in this step. The motivation for diameter correction is shown in Figure 12.

Figure 12a shows a fiber in an enlarged section of the preprocessed image before applying the segmentation step (step 2). The red line indicates the width of the actual fiber diameter. Figure 12b shows the image resulting after segmentation: clearly, the diameter that can be measured through the segment shift procedure described at step 4 is smaller than the actual diameter. This is due to the fact that the fiber has a cylindrical shape: the pixels representing fiber edges have a much smaller intensity than the fiber core pixels and, after segmentation, they are assigned to background rather than to fibers. Therefore, in order to provide a correct diameter measurement, the fiber edge thickness must be added to the preliminary diameter measurement.

The thickness of the fiber edges was determined using a derivative filter[42] coupled to a cluster analysis to separate the fiber edges from the rest of the image. Figure 10e shows the result of such operation: the fiber edges show up (they are highlighted in white) and their thickness can be measured; to this purpose, a distance-transform method[43] was applied. For each fiber, the preliminary diameter measurement can then be corrected by considering the relevant edge thickness, and the actual diameter measurement can therefore be determined at the end of this step.

3.5.6. Step 6: Perspective Correction. Recall from Figure 7 that only the first two pixel clusters were used to reconstruct the nanofiber image. These two clusters correspond to the fibers lying in the first two layers of the nanofiber web. By assuming that the membrane is homogeneous, it is expected that the fiber diameter distribution on each of these two layers is approximately the same.

The diameter measurement procedure described so far can provide a correct diameter measurement for the fibers belonging to the first (i.e. upper) layer only. Due to perspective effects, fibers lying on the second layer are displayed with a smaller diameter, and therefore the measurement of their diameter should be further corrected to take this issue into account.
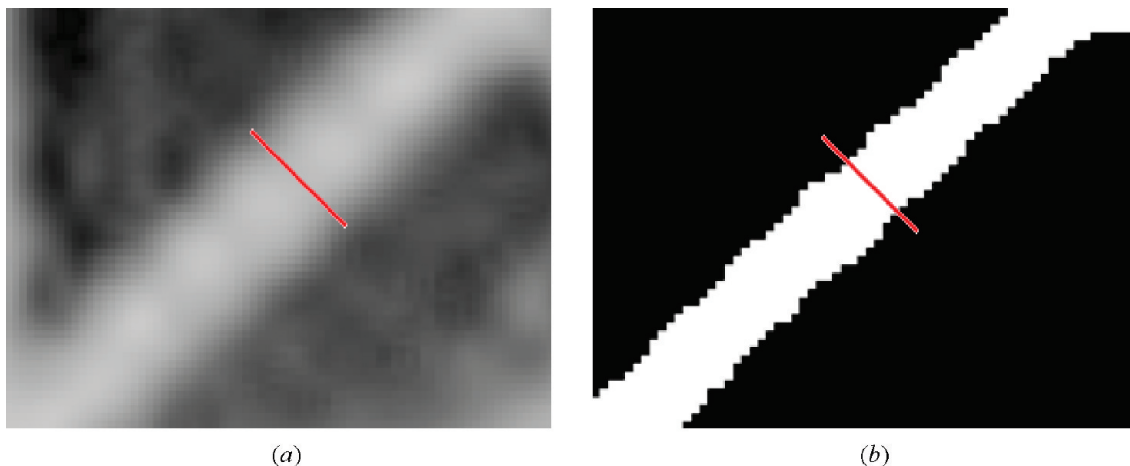
(*a*)

(*b*)

Figure 12. Detailed view of a single fiber in the original image (a) after image preprocessing and (b) after image segmentation. The red line represents the diameter of the sample fiber.

Using the results of MIA, all the fibers appearing in a subimage were assigned to either the first or the second layer, depending on the membership of their pixels. Figure 10f (which uses the same color coding as Figure 7) shows the result of this operation: if the fraction of yellow pixels in a fiber is larger than a threshold value (which was taken to be 0.7), the fiber is assigned to the first layer; otherwise it is assigned to the second one. A distribution can then be built for the diameters of each layer. The ratio between the two mean diameters is taken as the scaling factor, and the second-layer diameters can be scaled by this factor. Finally, the overall diameter distribution can be calculated.

4. Results and Discussion

4.1. Pore Diameter Distributions. For the membrane represented in Figure 3 the relative open area results 24.3%. The distributions of the measured interfiber pore shape parameters are shown in Figure 13.

The distributions of shape parameters looks like a gamma distribution. This agrees with the theoretical results of Johnston[44] and of Eichhorn and Sampson,[45] who demonstrated that the most probable distribution of the diameters of pores created by the intersections of random lines lying on a plane is a gamma distribution, in which the ratio of the standard deviation to the mean of the distribution (i.e., the coefficient of variation, CV) is $1/2^{1/2} \approx 0.707$, regardless of the average pore size. In the present case study, the values of CV for the equivalent diameter distribution, the hydraulic diameter distribution, and the ellipse major and minor axis distributions are all reasonably close to 0.707. The statistical values for distributions in Figure 13 are listed in Table 2.

Although the information that can be extracted from the interfiber pore morphology characteristics reported in Figure 3 and Table 2 is somewhat different from that provided by classical porosity measurements (and therefore has no direct experimental counterpart), the results provided by the automatic pore morphology characterization system can indeed provide objective and accurate information on the performance of a nanofiber membrane.

4.2. Fiber Diameter Distributions. The distribution of the measured fiber diameters for the sample image of Figure 3 is shown in Figure 14. Figure 14a refers to the case where the automatic fiber diameter measurement is carried out neglecting perspective effects, whereas the perspective correction is con-

sidered in Figure 14b. Finally, in Figure 14c the distribution of diameters measured manually from the nanofiber image is shown.

It can be noted that considering the perspective correction shifts the distribution mean to a larger value (see also Table 3) and makes the diameter distribution more compact. This fact is also emphasized by the CV value computed on the distributions and reported in Table 3: the first distribution (Figure 14a) is more scattered with respect to the mean of the distribution (CV = 0.356) compared to the second one (Figure 14b, CV = 0.308). Furthermore, the second distribution is much closer to a normal one, as one would conjecture.

Table 3 also shows that the difference between the means of the two first distributions is ~81 nm. Since 1 pixel corresponds to ~38.5 nm (which is therefore the resolution threshold for the images considered in this study), it can be concluded that neglecting the effect of perspective causes the loss of about 2 pixels. The third distribution (Figure 14c) confirms that the manual measurement seems to underestimate the fiber diameter. The difference between the means of Figure 14b and 14c is ~96 nm, i.e., above the resolution threshold and ~15% of the value measured automatically. Instead, the manual measurement provides a mean diameter that is very similar to the automatic one when no perspective correction.

Table 3 also indicates that the automatic procedure is able to take measurements on a much larger number of fiber diameters with respect to the manual one (255 fibers vs 152 fibers). Thanks to the larger number of samples, the distribution computed automatically is supposed to be more realistic in addition to quicker to obtain.

5. Conclusions

In this paper an artificial vision system has been proposed to characterize the morphology of electrospun nanofiber assemblies. This system uses an SEM image of the membrane to characterize the nanofiber assembly by automatically measuring several properties related to the interfiber pore distribution and to the nanofiber diameter distribution. The ability of the proposed automatic system in characterizing the morphology of a nanofiber web has been demonstrated by application to polymer nanofiber membranes obtained by electrospinning.

The artificial vision system is characterized by a two-section structure: an image processing section and a property measurement section. The image processing section uses wavelet filtering
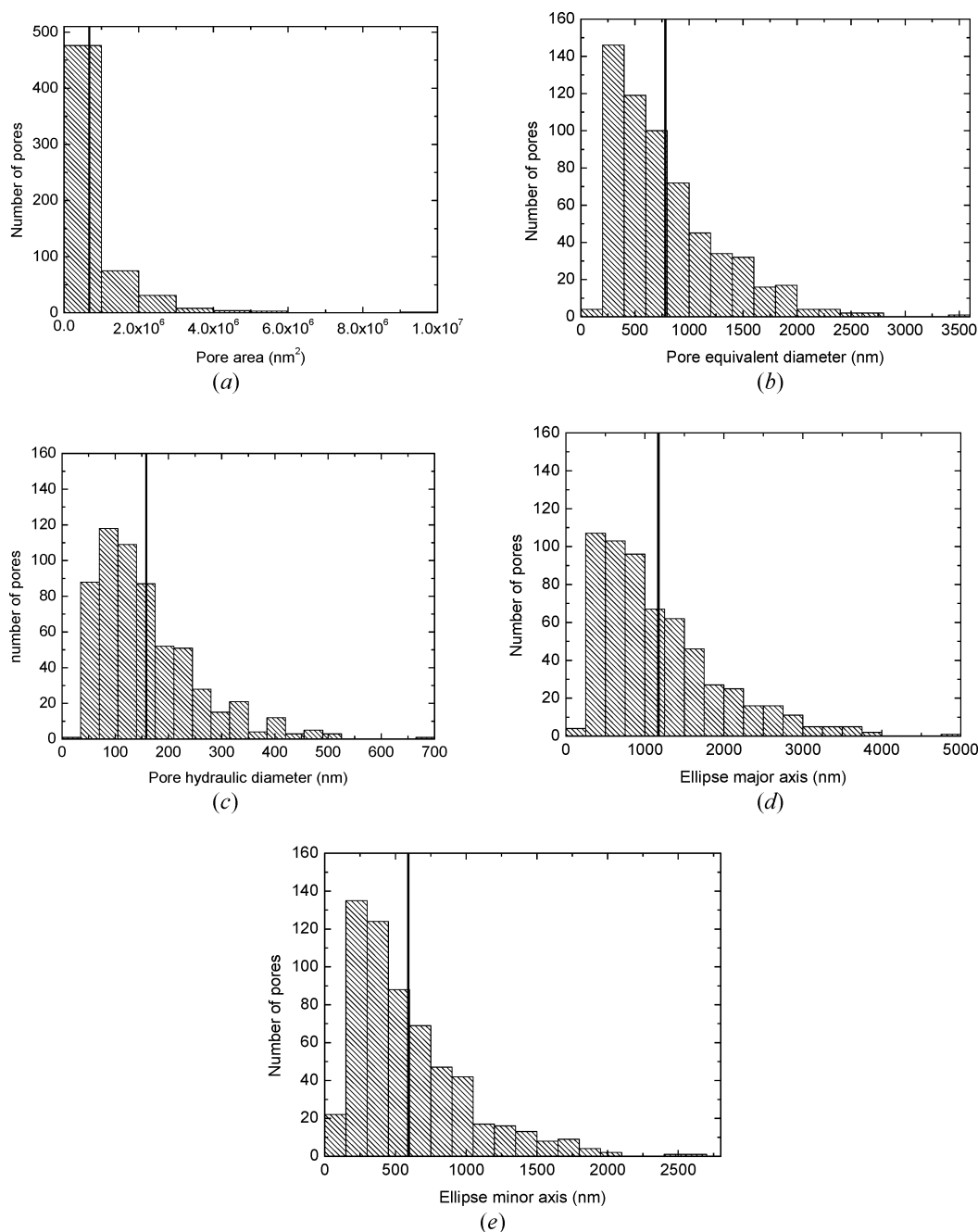
Figure 13. Distributions of some morphological parameters of pores for the membrane of Figure 3: (a) area, (b) equivalent diameter, (c) hydraulic diameter, and (d) major and (e) minor axes of the ellipse with the same normalized second central moment of the pore region. The vertical line in each diagram represents the mean of the distribution.

Table 2. Interfiber Pore Morphology Characterization: Parameters Computed from the Distributions of Figure 13

	area (μm^2)	equivalent diam (nm)	hydraulic diam (nm)	ellipse major axis (nm)	ellipse minor axis (nm)
mean	0.6735	781.5	158.2	1172.8	590.4
standard deviation	0.9141	497.2	96.0	764.5	405.1
CV	1.357	0.636	0.607	0.652	0.686

for image enhancement and is centered on a multivariate image analysis procedure for morphological feature extraction. By application of multiway principal component analysis on a spatially shifted version of the image,[20] the image is compressed to a low-dimensional latent space where pores and fibers lying on different layers can be separated through cluster analysis. The image is then reconstructed by keeping only the main features identified on the latent variable space.

The property measurement section comprises an algorithm for pore relative open area and pore morphology measurement and one for fiber diameter distribution determination. The first algorithm associates the pore characteristics with the characteristics of background areas as identified through MIA, and is able to provide the values for the pore area, pore equivalent diameter, pore hydraulic diameter, and length of the major and minor axes of the ellipse having the same normalized second central moment as the pore.

The second algorithm is able to identify each single fiber existing on the first two deposited layers of the nanofiber web, which allows measurement of the fiber diameters and their distribution, also accounting for the effect of perspective on the lower-layer-fiber diameters.
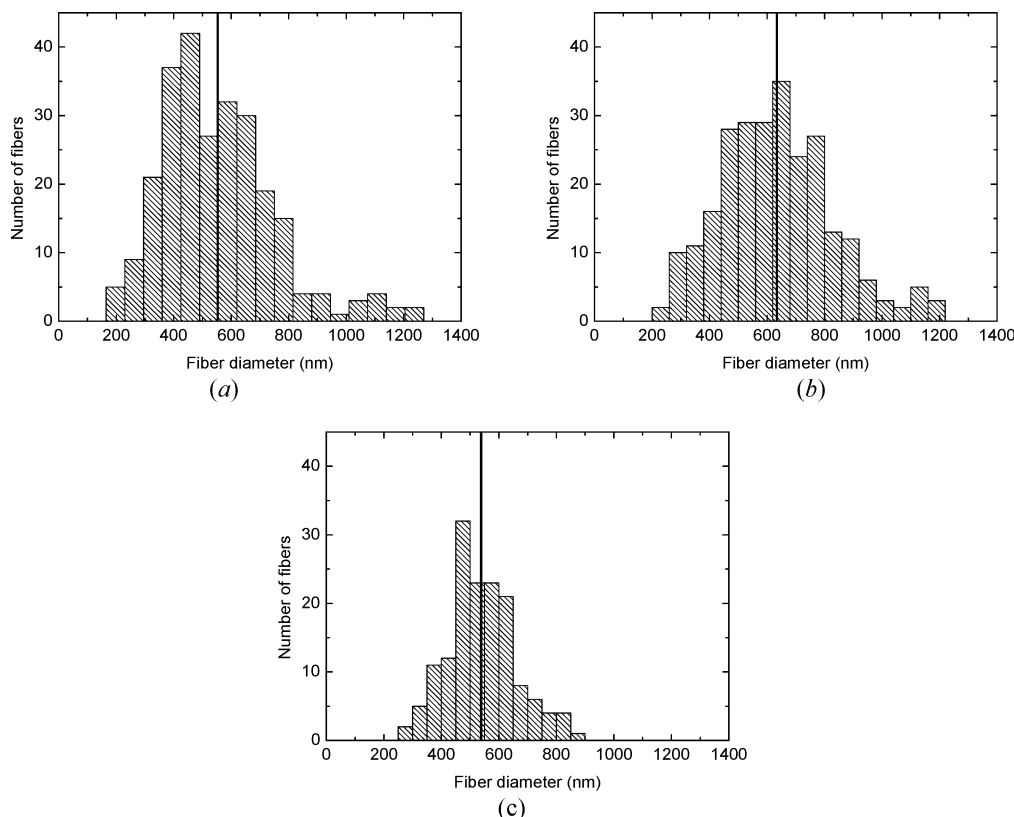
Figure 14. (a) Fiber diameter distribution for the membrane of Figure 3 without considering perspective effects. (b) Fiber diameter distribution after considering perspective effects. (c) Fiber diameter distribution from manual measurement from the image. The vertical line in each histogram represents the distribution mean.

Table 3. Fiber Diameter Measurement: Parameters Computed from the Distributions of Figure 14

	mean (nm)	standard deviation (nm)	CV	no. of analyzed fiber diameters
Figure 14a	552.7	196.7	0.356	257
Figure 14b	633.8	195.0	0.308	255
Figure 14c	538.3	118.2	0.220	152

Because the proposed artificial vision system is completely automatic, property measurements can be taken without the need for any experimental setup and with no human intervention. Therefore, they do not suffer from reproducibility issues. The calculation times are reasonably short: on an Intel Core 2 Quad Q6600/2.4 GHz with 4 GB RAM personal computer, it takes ~65 s to measure the pore characteristics and ~650 s to measure the fiber diameter characteristics. The algorithms have not been optimized from the numerical point of view, and therefore we believe that there is room for significant improvements in the calculation times.

Some limitations to the proposed technique are worth mentioning at this point. First, both the pore characteristics and the fiber diameter characteristics can be measured by the artificial vision system only if the nonwoven membrane is homogeneous, that is, if the analyzed image is representative not only of any location on the membrane surface, but also of fiber layers that are deposited at a deeper level. Then, the pore relative open area can be directly related to porosity only under the assumption that the membrane has a high packing density. Furthermore, accounting for perspective effects to correct the measured relative open area of pores is still an open issue. The accuracy of fiber diameter measurements is limited by two factors. The first one is the resolution of the available image. The images used in this study had a resolution of 1024 × 1280

pixels, which set a resolution threshold at 38.5 nm. This means that very thin fiber diameters cannot be measured accurately if this kind of image is available. However, using higher resolution images can considerably shorten the resolution threshold. The second issue is related to the algorithm for single fiber detection: if two fibers overlap for their entire length within one of the subimages being analyzed, the algorithm may assume that only one large-diameter fiber exists. This issue can be attenuated by carrying out the fiber diameter measurement on several subimages, which lowers the chance to encounter two fibers entirely overlapping within the whole image scene. Overcoming these limitations provides a driver for future research in this area.

Literature Cited

(1) Gopal, R.; Kaur, S.; Yang Feng, C.; Chan, C.; Ramakrishna, S.; Tabe, S.; Matsuura, T. Electrospun Nanofibrous Polysulfone Membranes as Pre-Filters: Particulate Removal. *J. Membr. Sci.* **2007**, *289*, 210.

(2) Jia, H.; Zhu, G.; Vugrinovich, B.; Kataphinan, W.; Reneker, D. H.; Wang, P. Enzyme-Carrying Polymeric Nanofibers Prepared via Electrospinning for Use as Unique Biocatalysts. *Biotechnol. Prog.* **2002**, *18*, 1027.

(3) Roso, M.; Sundarrajan, S.; Pliszka, D.; Ramakrishna, S.; Modesti, M. Multifunctional Membranes Based on Spinning Technologies: the Sinergy of Nanofibers and Nanoparticles. *Nanotechnology* **2008**, *19*, 1.

(4) Min, B.-M.; Lee, G.; Kim, S. H.; Nam, Y. S.; Lee, T. S.; Park, W. H. Electrospinning of Silk Fibroin Nanofibers and Its Effect on the Adhesion

and Spreading of Normal Human Keratinocytes and Fibroblasts in Vitro. *Biomaterials* **2004**, *25*, 1289.

(5) Agarwal, S.; Wendorff, J. H.; Greiner, A. Use of Electrospinning Technique for Biomedical Applications. *Polymer* **2008**, *49*, 5603.

(6) Kenawy, E.-R.; Abdel-Hay, F. I.; El-Newehy, M. H.; Wnek, G. E. Processing of Polymer Nanofibers through Electrospinning as Drug Delivery Systems. *Mater. Chem. Phys.* **2009**, *113*, 296.

(7) Kim, J.-S.; Reneker, D. H. Mechanical Properties of Composites Using Ultrafine Electrospun Fibers. *Polym. Compos.* **1999**, *20*, 124.

(8) Gibson, P.; Schreuder-Gibson, H.; Rivin, D. Transport Properties of Porous Membranes Based on Electrospun Nanofibers. *Colloids Surf.* **2001**, *187−188*, 469.

(9) Wang, X.; Drew, C.; Lee, S.-H.; Senecal, K. J.; Kumar, J.; Samuelson, L. A. Electrospun Nanofibrous Membranes for Highly Sensitive Optical Sensors. *Nano Lett.* **2002**, *2* (11), 1273.

(10) Jena, H.; Gupta, K. Pore Volume of Nanofiber Nonwovens. *Int. Nonwoven J.* **2005**, *14* (2), 25.

(11) Li, D.; Frey, M. W.; Joo, Y. L. Characterization of Nanofibrous Membranes with Capillary Flow Porometry. *J. Membr. Sci.* **2006**, *286*, 104.

(12) Gomes, D. S.; da Silva, A. N. R.; Morimoto, N. I.; Mendes, L. T. F.; Furlan, R.; Ramos, I. Characterization of an Electrospinning Process using Different PAN/DMF Concentrations. *Polim.: Cienc. Tecnol.* **2007**, *17*, 206.

(13) She, F. H.; Tung, K. L.; Kong, L. X. Calculation of Effective Pore Diameters in Porous Filtration Membranes with Image Analysis. *Rob. Comput.-Integr. Manuf.* **2008**, *24*, 427.

(14) Ziabari, M.; Mottaghitalab, V.; Haghi, A. K. Distance Transform Algorithm for Measuring Nanofiber Diameter. *Korean J. Chem. Eng.* **2008**, *25* (4), 905.

(15) Ziabari, M.; Mottaghitalab, V.; Haghi, A. K. Evaluation of electrospun nanofiber pore structure parameters. *Korean J. Chem. Eng.* **2008**, *25* (4), 923.

(16) Ziabari, M.; Mottaghitalab, V.; Haghi, A. K. Application of direct tracking method for measuring electrospun nanofiber diameter. *Braz. J. Chem. Eng.* **2009**, *26*, 53.

(17) Geladi, P.; Grahn, H. *Multivariate Image Analysis*; John Wiley & Sons: New York, 1996.

(18) Bharati, M. H.; MacGregor, J. F. Multivariate Image Analysis for Real-Time Process Monitoring and Control. *Ind. Eng. Chem. Res.* **1998**, *37*, 4715.

(19) Yu, H.; MacGregor, J. F. Multivariate Image Analysis and Regression for Prediction of Coating Content and Distribution in the Production of Snack Foods. *Chemom. Intell. Lab. Syst.* **2003**, *67*, 125.

(20) Bharati, M. H.; Liu, J. J.; MacGregor, J. F. Image Texture Analysis: Methods and Comparisons. *Chemom. Intell. Lab. Syst.* **2004**, *72*, 57.

(21) Liu, J. J.; MacGregor, J. F.; Duchesne, C.; Bartolacci, G. Flotation Froth Monitoring Using Multiresolutional Multivariate Image Analysis. *Miner. Eng.* **2005**, *18*, 65.

(22) Prats-Montalbàn, J. M.; Ferrer, A. Integration of Colour and Textural Information in Multivariate Image Analysis: Defect Detection and Classification Issues. *J. Chemom.* **2007**, *21*, 10.

(23) Sarkar, D.; Doan, X.-T.; Ying, Z.; Srinivasan, R. In Situ Particle Size Estimation for Crystallization Processes by Multivariate Image Analysis. *Chem. Eng. Sci.* **2009**, *64*, 9.

(24) Andrady, A. L. *Science and Technology of Polymer Nanofibers*; John Wiley & Sons: New York, 2008.

(25) Ramakrishna, S.; Fujihara, K. *An Introduction to Electrospinning and Nanofibers*; World Scientific Publishing Co.: Singapore, 2005.

(26) Shin, Y. M.; Hohman, M. M.; Brenner, M. P.; Rutledge, G. C. Electrospinning: A whipping fluid jet generates submicron polymer fibers. *Appl. Phys. Lett.* **2001**, *78*, 1149.

(27) Reneker, D. H.; Yarin, A. L.; Fong, H.; Koombhongse, S. Bending instability of electrically charged liquid jets of polymer solutions in electrospinning. *J. Appl. Phys.* **2000**, *87*, 4531.

(28) Addison, P. S. *The Illustrated Wavelet Transform Handbook*; Taylor & Francis: New York, 2002.

(29) Maksumov, A.; Vidu, R.; Palazoglu, A.; Stroeve, P. Enhanced feature analysis using wavelets for scanning probe microscopy images of surfaces. *J. Colloid Interface Sci.* **2004**, *272*, 365.

(30) Mallat, S. G. A theory for multiresolution signal decomposition: the wavelet representation. *IEEE Trans. Pattern Anal. Mach. Intell.* **1989**, *11*, 674.

(31) Facco, P.; Mukherjee, R.; Bezzo, F.; Barolo, M.; Romagnoli, J. A. Monitoring Roughness and Edge Shape on Semiconductors through Multiresolution and Multivariate Image Analysis. *AIChE J.* **2009**, *55*, 1147.

(32) Sun, W.; Romagnoli, J. A.; Tringe, J. W.; Létant, S. E.; Stroeve, P.; Palazoglu, A. Line Edge Detection and Characterization in SEM Images Using Wavelets. *IEEE Trans. Semicond. Manuf.* **2009**, *22*, 180.

(33) Salari, E.; Ling, Z. Texture Segmentation Using Hierarchical Wavelet Decomposition. *Pattern Recognit.* **1995**, *28*, 1818.

(34) Ruttimann, U. E.; Unser, M.; Rowlings, R. R.; Rio, D.; Ramsey, N. F.; Mattay, V. S.; Hommer, D. W.; Frank, J. A.; Weinberger, D. R. Statistical Analysis of Functional MRI Data in the Wavelet Domain. *IEEE Trans. Med. Imaging* **1998**, *17*, 142.

(35) Kourti, T.; MacGregor, J. F. Process Analysis, Monitoring and Diagnosis, Using Multivariate Projection Methods. *Chemom. Intell. Lab. Syst.* **1995**, *28*, 3.

(36) Wold, S.; Geladi, P.; Esbensen, K.; Öhman, J. Multi-way principal components and PLS-analysis. *J. Chemom.* **1987**, *1*, 47.

(37) Hartigan, J. A.; Wong, M. A. A K-Means Clustering Algorithm. *Appl. Stat.* **1979**, *28*, 100.

(38) Dierickx, W. Opening size determination of technical textiles used in agricultural applications. *Geotext. Geomembr.* **1999**, *17*, 231.

(39) Mathworks. *Matlab: The Language of Technical Computing−Image Processing Toolbox*, version 6.0; The MathWorks Inc.: Natick, MA, 2008.

(40) Johnston, P. R. *Fluid Sterilization by Filtration*, 3rd ed.; Interpharm/CRC: Boca Raton, FL, 2004.

(41) Tomba, E. Multivariate Image Analysis Techniques for Quality Monitoring of Polymer Nanofiber Membranes (in Italian). Master's Thesis in Chemical Engineering, DIPIC, University of Padova, Italy, 2009.

(42) Gonzales, R. C.; Woods, R. E. *Digital Image Processing*; Prentice-Hall, Inc.: Upper Saddle River, NJ, 2002.

(43) Breu, H.; Gil, J.; Kirkpatrick, D.; Werman, M. Linear Time Euclidean Distance Transform Algorithms. *IEEE Trans. Pattern Anal. Mach. Intell.* **1995**, *17*, 529.

(44) Johnston, P. R. Revisiting the Most Probable Pore Size Distribution in Filter Media: the Gamma Distribution. *Filtr. Sep.* **1998**, *35*, 287.

(45) Eichhorn, S. J.; Sampson, W. W. Statistical Geometry of Pores and Statistics of Porous Nanofibrous Assemblies. *J. R. Soc. Interface* **2005**, *2*, 309.